Authors: I. Boxx, C.D. Carter, W.Meier

Title: "On the Feasibility of Tomographic-PIV With Low Pulse-Energy Illumination in a Lifted Turbulent Jet Flame"

Journal: Experiments in Fluids, 55:1771 (2014)

On the Feasibility of Tomographic-PIV With Low Pulse-Energy Illumination in a Lifted Turbulent Jet Flame

I. Boxx, C.D. Carter, W. Meier

Abstract

Tomographic particle image velocimetry (tomographic-PIV) is a recently developed measurement technique used to acquire volumetric velocity field data in liquid and gaseous flows. The technique relies on line-of-sight reconstruction of the rays between a 3D particle distribution and a multi-camera imaging system. In a turbulent flame, however, index-of-refraction variations resulting from local heat-release may inhibit reconstruction and thereby render the technique infeasible. The objective of this study was to test the efficacy of tomographic-PIV in a turbulent flame. An additional goal was to determine the feasibility of acquiring usable tomographic-PIV measurements in a turbulent flame at multi-kHz acquisition rates with current generation laser and camera technology. To this end, a setup consisting of four CMOS cameras and a dual-cavity Nd:YAG laser was implemented to test the technique in a lifted turbulent jet flame. While the cameras were capable of kHz-rate image acquisition, the laser operated at a pulse repetition rate of only 10 Hz. However, use of this laser allowed exploration of the required pulse energy and thus power for a kHz-rate system. The imaged region was $29 \times 28 \times 2.7$mm in size. The tomographic reconstruction of the 3D particle distributions was accomplished using the multiplicative algebraic reconstruction technique. The results indicate that high quality tomographic-PIV measurements in a turbulent flame are possible with laser pulse energies of 25mJ, which is within the capability of current-generation kHz-rate diode-pumped solid state lasers.

Introduction

Fluid dynamic strain is a key driver of turbulent flame dynamics. It results from velocity gradients in the turbulent flow and therefore may occur in any direction. The full velocity gradient tensor has nine elements, corresponding to gradients in each of the three components of velocity. A key limitation in the study of turbulent flames is the inability of current measurement techniques to resolve all nine elements of the velocity gradient tensor simultaneously. The widely used stereoscopic particle image velocimetry (PIV) technique [Adrian, 1991; Prasad, 2000; Raffel et al., 1998] provides access to up to six elements of the tensor simultaneously in a plane but is unable to capture gradients perpendicular to the imaging plane. Researchers have attempted to address this limitation in various ways, usually via assumptions such as flow symmetry, global isotropy or the alignment of the flame orthogonal to the axis of in-plane principal compressive strain. Others have attempted to address the problem directly by acquiring multiple planes of PIV data simultaneously or by acquiring data in a single plane with sufficient temporal resolution to enable a 3D reconstruction of the flow that has passed through it. For example, Pfadler et al. [2009, 2010] applied stereoscopic-PIV simultaneously in two parallel planes to measure the full nine-component strain-rate tensor in a premixed turbulent V-flame. This technique, while feasible in some flames, provides a relatively coarse, two-point approximation to the velocity gradient in the z-direction. As this method is based on linear interpolation of velocities measured in two separate, parallel laser sheets, it is also sensitive to misalignment of the laser sheets and to beam-steering resulting from index-of-refraction variations throughout the flowfield. Ganapathisubramani et al. (2008) describes an alternate approach wherein high frequency (kHz-framerate) stereoscopic-PIV is applied in a plane perpendicular to the axial flow direction of a gaseous jet, and Taylor's frozen flow hypothesis is used to reconstruct the quasi-instantaneous, 3D distribution of the velocity field that propagates through it. This technique has since been applied to study turbulence-flame interaction in premixed [Steinberg et al., 2009] and non-premixed [Gamba et al., 2013] turbulent flames. This technique, while robust and relatively straightforward to implement experimentally, is of limited utility in understanding the dynamics of turbulence-flame interaction, as it produces only quasi-instantaneous velocity field reconstructions.

Tomographic particle image velocimetry (tomographic-PIV) is a recently developed, 3D measurement technique [Elsinga et al, 2006, Scarano, 2013], wherein multiple cameras are used to image tracer particles in a flow from several viewing angles simultaneously. With volumetric illumination and the use of objective lenses with sufficient depth of field (set by camera lens f-number setting) to keep the particles in focus throughout the illuminated region, it is possible to reconstruct the 3D distribution of tracer particles using optical tomography. The resulting particle distributions are then cross-correlated in a manner similar to conventional PIV to obtain 3D velocity fields. Tomographic PIV has advantages over conventional PIV in that it provides three velocity components throughout a volume from which a complete set of derivative quantities such as strain and vorticity can be derived. The development of diode-pumped solid state (DPSS) lasers and highspeed complementary metal oxide semiconductor (CMOS) cameras has since enabled researchers [Schroeder et al., 2008; Violato et al., 2010] to acquire tomographic-PIV in non-reacting flows at rates up to 5 kHz. Application of tomographic-PIV at kHz acquisition rates yields time-series measurements of the aforementioned turbulence quantities. KHz acquisition-rate tomographic-PIV thus has the potential to revolutionize our understanding turbulence-chemistry interaction in turbulent-flames, where these quantities play a dominant role. Significant technical challenges, however, must be addressed if the potential of this measurement technique is to be realized in the challenging environment of a turbulent flame.

The tomographic-PIV technique has only been fully characterized in non-reacting liquid and gaseous flows. Researchers have recently begun to attempt tomographic-PIV in reacting

flows, but to date there has been no rigorous or systematic study of the feasibility and limitations of this measurement technique in a turbulent flame. Lecordier et al. (2012) reports accomplishing tomographic-PIV measurements in a LJF of methane. In that study, the jet and co-flowing air stream were seeded with oil droplets and illuminated with 400mJ of pulsed laser illumination, which was retro-reflected a single time using a mirror. The study provides no information on basic PIV parameters such as particles per interrogation box (particularly in the burnt-gas region), correlation strength or at what temperature their seed particles (oil droplets) evaporate. Petersson et al., (2013) report the application of tomographic-PIV in a lifted turbulent premixed low-swirl flame. This study reports achieving a 50 × 45 × 20mm measurement volume but neglects to mention basic information such as vector resolution, pulse energy of the laser illumination, particles per interrogation box or correlation strength. Coriton et al., (2013) report having accomplished tomographic-PIV in a partially-premixed LJF of dimethyl ether at 10kHz, with 12mJ pulsed laser illumination over a region of 17 × 11.5 × 3.4mm, with a resolution of 0.36mm^3 / vector. While these results are impressive, this conference paper gives little information regarding checks on the quality of either the 3D particle reconstruction or the resulting velocity field measurement. Taken together, these studies do not provide a firm foundation upon which to judge the viability of tomographic-PIV as a robust and reliable measurement technique in turbulent flame. The aim of present work is to thoroughly test the feasibility of accomplishing tomographic-PIV in a turbulent jet flame and to determine the feasibility of doing so at kHz acquisition-rates using commercially available cameras and lasers.

Background

Technical challenges to kHz-rate tomographic-PIV in a turbulent flame

Index-of-refraction variations resulting from combustion heat release provide the key technical challenge to accomplishing tomographic-PIV in a turbulent flame. Redirection of optical rays resulting from a variation in the index-of-refraction associated with the flame complicate both the illumination of the measurement volume and the tomographic reconstruction of the 3D particle distributions.

It has been demonstrated [Schöder et al., 2008] that high-quality tomographic-PIV measurements in a non-reacting air flow seeded with 1.5μm diameter fog droplets can be accomplished over an area of 34 × 30 × 19mm at 5 kHz with 21mJ of pulsed laser illumination. Ghaemi and Scarano (2011) recently showed it is possible to obtain high quality tomographic-PIV measurements in a non-reacting air flow seeded with 1μm diameter fog droplets over an area as large as 47 × 47 × 8 mm at 2.7 kHz with just 13mJ of pulsed laser illumination. In both cases, however, this required the use of a light amplification system consisting of mirrors placed on either side of the measurement system to reflect the beam repeatedly through the measurement volume. Redirection of the illumination beam as a result of index-of-refraction variations across a reacting flowfield will inevitably degrade the performance of such systems. Without being able to rely on multi-pass light amplification cells, it is not clear whether the ≈20 – 50mJ pulse energies available from current generation commercial DPSS laser systems is sufficient for acquisition of high quality tomographic-PIV measurement.

Index-of-refraction variations across a flame may also impede the tomographic reconstruction of 3D particle distributions. Tomographic reconstruction requires that linear (line-of-sight) rays between particles in the measurement volume and their projected 2D images on the camera arrays intersect at a discrete point in space. Successful triangulation of the particle location therefore requires that these rays intersect to within a fraction of the diameter of the projected particle image. Successful reconstruction of particle distributions depends on a spatial calibration accurate to within 0.4 pixels [Elsinga et al., 2006]. Through

careful calibration using a physical imaging target and subsequent application of a self-calibration routine based on cross-correlation of particles in an isothermal medium it is relatively straightforward to achieve a calibration accuracy of 0.1 pixels or better.

Distortion of the line-of-sight projection of particle images onto the imaging array has the potential to affect the accuracy of the geometric calibration. This effect has been studied for the case of 2- and 3-component planar PIV in flames by Muniz et al. (1996) and Han et al. (2000), respectively. Muniz et al. (1996) determined the effect "flame-induced" distortion to be negligible for two-component PIV, whereas Han et al. (2000) observed distortions ranging from 0.2 to 0.9 pixels in rays projected through a hydrogen jet-flame vs. those projected through a cold flow. Based on these estimates it is not clear whether a robust tomographic reconstruction of 3D particle distributions in a reacting flow is possible.

Experiment Configuration

In order to test the feasibility of accomplishing tomographic-PIV at kHz acquisition rates in a turbulent flame using only current-generation, commercially available technology we implemented a tomographic-PIV system subject to the illumination and imaging configuration constraints described above. The system was then used to study the stabilization region of a turbulent lifted jet flame (LJF) of methane in a low velocity air co-flow.

The experimental setup is shown schematically in Figure 1. The tomographic-PIV system consists of two components, the four-camera imaging system and the volumetric illumination system. These are described separately in the section below. The system was operated at 10Hz. The LJF burner and run conditions are described separately.

Illumination

The measurement volume was illuminated at 532nm by a dual-cavity, flashlamp-pumped Nd:YAG laser (New Wave Solo-PIV). Timing separation between laser pulses was set to 10 or 20 μs, depending on imaging location. The maximum pulse-energy of this laser is 120mJ. In the present study, neutral density filters were used to attenuate the pulse energy to either 25 or 40mJ, to enable assessment of the effect of pulse energy. This beam energies used were intended to duplicate the maximum pulse energy available from current-generation diode-pumped solid state (DPSS) lasers with multi-kHz repetition rates. The volumetric illumination optics consisted of a spherical-lens telescope, followed by a cylindrical-lens telescope. The spherical-lens telescope consisted of a pair of lenses, the first with a focal length of -82mm and the second with +150mm, to approximately double the initial beam diameter. The cylindrical-lens telescope was used to expand the beam vertically and collimate it. The telescope used a pair of lenses, the first of which had a focal length of -38mm and the second +250mm. The resulting beam was approximately 27mm tall. A set of knife-edges were used to block the low-intensity wings of the beam and thus prevent stray light from affecting the measurement. The knife edges were mounted 3mm apart, to limit the beam thickness to that width. A retro-reflecting mirror was used to pass the beam through the illuminated region a second time, and apertures placed in the beam path provide an easy means of aligning the retro-reflector.

Imaging System

Particle images were recorded on four CMOS cameras mounted in a linear array aligned on one side of the measurement volume. The outer two cameras of this array subtended an angle of 88 degrees, and the inner pair 28 degrees. Each camera had a 1024 × 1024 pixel imaging array and was equipped with a 200mm imaging objective (Nikon, AF-Nikkor) set to f/16. Each camera was coupled to its objective using a Scheimpflug adaptor, in order to correct for blurring caused by off-axis imaging. The Scheimpflug adaptors were configured such that the focus plane of each camera was aligned to the center of the measurement volume. Two of the

cameras, both LaVision HSS5 models, were capable of full-frame acquisition rates of up to 3000 fps, and the arrays were digitized with 10-bit resolution. The two remaining cameras, LaVision HSS6 and HSS8 models, were capable of full-frame imaging at 5000 and 7500 fps, respectively, and the arrays were digitized with 12-bit resolution. These cameras have CMOS imaging arrays with sizes and pixel dimensions similar to the current state-of-the-art in this field. Nonetheless, newer camera models are available that have higher maximum readout rates (up to about 20,000 fps) and improved sensitivity. The dimensions of the measurement volume were 29 × 28 × 2.7 mm. Images were acquired at three imaging locations, including one at the jet-centerline beginning 8mm downstream of the jet-exit and two in the vicinity of the flame leading edge, beginning approximately 42 mm downstream of the jet-exit.

The cameras were operated in full-frame imaging mode, synchronized to the laser via a digital delay generator (Quantum Composers 9528) and a timing synchronization / control module (LaVision Highspeed Controller). The minimum acquisition rate of the cameras was 60Hz. The cameras were therefore operated in full-frame imaging mode at that frequency, resulting in a dual-frame imaging rate of 30 Hz and single-frame exposure times of 16.7ms. The 10Hz repetition rate of the laser resulted in every third dual-frame image of the sequence being illuminated. The onboard memory of the cameras enabled the acquisition of 1024 image pairs per imaging run. As only one third of these images were illuminated, 341 dual-frame tomographic-PIV measurements were acquired per imaging run.

Jet-flame Burner

The axisymmetric jet flame burner consists of an 8mm inner diameter fuel tube, which supplies a jet of methane with 16.5m/s mean velocity at the exit. The fuel tube is tapered from 10mm outer diameter to a sharp edge at the jet-exit. The fuel jet is surrounded by a concentric nozzle of 140mm diameter. This nozzle is preceded by a settling chamber and a series of perforated plate flow-conditioning elements. It supplies a low-speed (310 g/min, or 0.27 m/s mean velocity) co-flow of air to ensure stable and reproducible boundary conditions at the lifted flame base. Both the jet and the co-flow were seeded with titanium dioxide particles with a nominal mean diameter of 1 μm. Flow rates of the fuel and co-flow air were monitored throughout the experiment via calibration-standard Coriolis mass flowmeters (Siemens Sitrans-FC Mass-Flo 2100, model DI-3 and DI-15 respectively).

Data Processing

Image pre-processing

A series of pre-processing steps was applied to the particle images prior to tomographic reconstruction of the 3D particle distributions. The effect of each pre-processing step is illustrated in Figure 2. First, a 3 × 3 pixel sliding minimum subtraction was applied, to remove the diffuse flame luminosity. Next, the images were normalized to the 100 × 100 pixel local average, to reduce the effect of illumination nonuniformity. The intensity distributions of all four cameras were then normalized to a single value. To improve contrast in the low seed-particle density regions around the flame, a Gaussian filter (window size 3×3 pixel), followed by a sharpening filter was applied. To further improve contrast and reduce the effect of camera fixed-pattern noise, a constant intensity (10 counts) was subtracted from each pixel. Finally, the pre-processed image was multiplied by a constant, to reduce the effect of rounding error when the particle images are stored in integer format prior to tomographic reconstruction.

Volumetric Calibration

Volumetric calibration was accomplished by acquiring a series of five images of a dual-plane imaging target (LaVision Type 7) that was traversed through the PIV measurement volume on a micrometer-actuated translation stage. Each target image consisted of an ensemble-average of 100 frames (to ensure good signal-to-noise ratio for the target images) acquired from the corresponding camera. Displacement of the target from image to image was 1mm in the z- (through-plane) direction. The Type 7 dual-plane calibration target has circular reference dots separated by 5mm on each plane and a planar separation of 1mm. The calibration images therefore contained between 25 and 36 calibration points on each plane, depending upon z-location. Based on these images, a volumetric calibration was performed using a pinhole camera model implemented in a commercial PIV analysis package (LaVision Davis 8.1). The accuracy of the initial mapping function was between 0.4 and 1.2 pixels, depending on the camera. This mapping function was then refined using volumetric self-calibration (Weineke, 2008) to achieve a mapping function accurate to within 0.02 pixels at the beginning of day. Volumetric self-calibrations performed on each subsequent run of the non-reacting flow indicate this calibration drifts to as much as 0.32 pixels accuracy by the end of the day. As this is still within the 0.4 pixel accuracy specified in Elsinga et al. (2006), a single volumetric calibration was used for each day of imaging runs. In this study, a new multi-plane calibration and self-calibration procedure were performed daily. The drift in calibration accuracy over the course of the day may be corrected by periodic acquisition of new sets of images of low seed-density flow throughout the day to enable repeated volumetric self-calibrations, possibly as often as prior to each measurement run in a flame.

Volumetric Reconstruction and Cross-correlation

Reconstruction of the 3D particle distributions was accomplished using the multiplicative algebraic reconstruction technique (MART – Elsinga et al., 2006), with 10 iterations. The resolution of the particle image reconstructions is 37.7 voxels / mm. The reconstructed volume measures $29 \times 28.2 \times 6$ mm, or $1096 \times 1062 \times 226$ voxels. Although the depth of the reconstructed volume is larger than the illuminated region (6mm vs 3mm), the additional reconstruction volume is a useful check on the quality of the tomographic reconstruction, as any particles reconstructed beyond the illuminated volume are clearly non-physical, or "ghost-particles". This effect will be discussed in greater detail in a later section of the paper.

Velocity field data was extracted from the reconstructed 3D particle distributions via an adaptive window offset, 3D particle cross-correlation algorithm. The initial window size for this correlation was $128 \times 128 \times 128$ voxels, and the final one was $64 \times 64 \times 64$, with 75% vector overlap. This corresponds to a vector resolution of approximately 1.7mm cubed, and vector spacing of 0.43mm. Spurious vectors were detected and removed via the universal outlier detection method proposed by Westerweel and Scarano (2005), and replaced with vectors corresponding to the average of the surrounding $3 \times 3 \times 3$ vectors. The resulting 3D velocity field data was then smoothed with a single-pass, $3 \times 3 \times 3$ Gaussian filter.

Results

The primary goal of the present study was to investigate the feasibility of performing tomographic-PIV in a turbulent, reacting flow and to judge the feasibility of doing so at kHz frame-rates using currently available laser and camera technology. The results and discussion presented below therefore focus primarily on those parameters relevant to judging the potential (and the limitations) of this measurement technique in reacting flows. The secondary goal, however, was to investigate the 3D velocity field associated with the canonical LJF.

Seed Particle Density

As with conventional (planar) PIV, the spatial resolution achievable with tomographic-PIV is strongly linked to the concentration of seed particles in the flow. It has been shown that for a robust cross-correlation, an interrogation box (IB) should contain at least 5-10 particles [Scarano, 2013]. It was well-established by Elsinga et al. (2006), however, that the percentage of ghost particles in a tomographic reconstruction increases with increasing seed particle concentration. They have shown that for a four-camera tomographic imaging system, the optimal seed particle concentration (i.e., the highest concentration that still produces a tomographic reconstruction of acceptable quality) is approximately 0.05 particles per pixel (ppp).

Seed particle counts (summarized in Table 1) were determined by applying an intensity threshold to binarize the (pre-preprocessed) seed-particle images and counting the number of particles in the frame. Particle concentrations were estimated with the assumptions that the seed particles were evenly distributed throughout the 28 × 28 × 3mm illuminated volume and that the values from a single camera frame were characteristic of the entire run and of each camera. With the same assumptions, the average number of particles in a 64^3 and a 32^3 voxel IB were estimated. The numbers given in Table 1 are thus best-estimate values. Nonetheless, they provide a useful basis for comparison between both prior studies and between individual run conditions in the present study. It is clear from Table 1 that the seed particle density (particles per pixel) in this study was below the optimal level of 0.05ppp observed by Elsinga et al. (2006). The estimated seed particle concentration (particles / mm^3), however, is higher than that typically reported for studies of non-reacting gaseous flows [Scarano, 2013]. Although seed particle concentrations are not typically reported in studies applying conventional PIV, concentrations greater than 0.05ppp are typically used to study turbulent flames in order to ensure sufficient seed particle concentration for robust cross-correlations in regions of both burned and unburned gas. Indeed, the drop in particle density is so clear that it is frequently used to identify the reaction zone in PIV studies of premixed turbulent flames [Pfadler et al., 2007]. The relatively high seed-particle concentration in the present study was intended to help ensure adequate seed concentration in low-density regions created by combustion heat-release.

Table 1 – Seed particle concentration

Run Condition	Particles (total)	ppp	Concentration (mm^{-3})	Particles per 64 voxel IB	Particles per 32 voxel IB
40mJ illumination, At jet-exit	34397	0.033	14.5	71	9
40mJ Non-reacting jet	26824	0.026	11.4	56	7
40mJ Lifted jet flame	35008	0.033	14.9	73	9
25mJ Non-reacting jet	18872	0.018	8	39	5
25mJ Lifted jet flame	32548	0.031	13.8	67	8

Table 1 shows that a 64^3 voxel IB contains, on average, ≈ 40 – 70 particles, i.e. significantly more than are required to achieve robust cross-correlations. Assuming the fluid reaches the adiabatic flame temperature of methane (ca. 2200K), the seed particle density will drop by a factor of approximately 7.5 in regions of the flame. Therefore, IBs in regions of burned gas are expected to contain 5-9 particles, which is still above the threshold required for robust cross-correlations. By comparison, a 32^3 voxel IB contains (on average) 5-9 particles in regions of unburned gas and < 2 particles in regions of burned gas. Therefore, while a 32^3 voxel IB may yield viable vectors in regions of unburned gas, it is clearly unsuitable for the

reacting flow condition. This is the basis for our decision to process the vectors with 64^3 voxel IB sizes.

Ghost Particles and SNR

A key measure of the quality of a tomographic particle reconstruction is the ratio of real-particles in a reconstructed volume to non-physical artifacts known as "ghost particles". Ghost particles in a tomographic PIV reconstruction occur as a result of the line-of-sight reconstruction between particles and the cameras [Maas et al., 1993]. It has been shown [Elsinga et al., 2006] that as the seed-particle density in a flow is increased the number of non-physical "ghost particles" in a tomographic reconstruction also increases. Ghost particles are effectively noise in the particle reconstruction and they decrease the contrast of the volumetric cross-correlation used to determine velocity fields.

Although we do not have a means by which to rigorously distinguish between real and ghost particles in the tomographic reconstructions, it is possible to quantify the contribution of each to the total measured signal level. We do this by comparing the mean integrated signal of the 3D particle reconstruction within and beyond the illuminated volume according to the relation,

$$\% \text{ Ghost Particle Signal} = (I_{ov})/(I_{iv} - I_{ov}) \qquad (1)$$

where I_{ov} is the integrated signal outside the illuminate volume, and I_{iv} is the integrated signal level within the illuminated volume. The reciprocal of this number may be interpreted as the signal-to-noise ratio (SNR) of the particle reconstruction.

Figure 3 shows profiles of the integrated signal intensity vs. z-direction for each laser beam. The upper row shows the non-reacting (left) and reacting (right) flow conditions with 40mJ illumination. The lower row shows them with 25mJ illumination. The profiles are integrated over the entire xy-imaging plane and averaged over a full imaging run of 341 measurements. Applying Eqn. 1, we find the SNR with 40mJ illumination is 19 – 26 for the non-reacting jet and 11 – 14 in the lifted jet flame. As expected, the SNR with 25mJ is lower, at 9 –10 for the non-reacting jet and 11 – 12 in the lifted jet flame. Nonetheless, this analysis indicates it is possible to accomplish tomographic reconstruction of 3D particle distributions with SNR well above the cutoff value of 2 [Scarano, 2013] required for good-quality tomographic-PIV, despite the presence of a flame in the line-of-sight of the imaging system.

Effect of the Flame on Calibration Accuracy

In a lifted turbulent jet flame, the reaction zone is known to reside in the low-velocity periphery of the jet [Muniz and Mungal, 1997]. The orientation of the measurement volume in this study is such that only a small portion of it is expected to contain regions of hot gas associated with the presence of a reaction zone. Nonetheless, the axisymmetric nature of the TLJF means that a flame sheet will frequently lie in the line-of-sight between the measurement volume and the cameras and is expected to influence the accuracy of the tomographic reconstruction of 3D particle fields. To quantify this effect, volumetric self-calibrations were computed for the reacting and non-reacting jet cases for each illumination level.

Table 2 lists the mean disparities between the volumetric calibrations computed during a measurement run and those at the beginning of the day. The reacting and non-reacting cases for each illumination level were acquired sequentially, to minimize calibration drift between measurement runs. Table 2 shows that the presence of a flame in the line-of-sight between the measurement volume and the cameras results in a measurable degradation on the accuracy of the volumetric calibration. At both illumination levels, the mean disparity between the start-of-day calibration and the calibration for that run increases significantly. As will be shown

later, in this study the effect is sufficiently small as to not inhibit the tomographic reconstruction of particle distributions. It is clear from Table 2, however, that this effect must be carefully considered in the design and implementation of tomographic-PIV measurements in a turbulent flame.

Table 3 – Effect of the flame on the volumetric calibration

Run Condition	Mean Disparity (Pixels)	RMS (Pixels)
40mJ Illumination Non-reacting jet	0.083	0.059
40mJ Lifted jet flame	0.19	0.089
25mJ Non-reacting jet	0.158	0.137
25mJ Lifted jet flame	0.321	0.09

Correlation Strength

Another measure of the quality of planar and tomographic PIV measurements is the ratio of the magnitudes of the first and second strongest peaks in the correlation map. A larger ratio is usually indicative of higher fidelity for the velocity measurement. Figure 4 shows the mean 1st-to-2nd correlation-peak ratio at the jet-centerline plane for the reacting and non-reacting jets. The upper row shows the case with 40mJ illumination and the lower, 25mJ. The left column shows the non-reacting jets and the right, the reacting jets. Although we do not have a direct measure of the mean flame location, prior research has shown that the leading-edge of the LJF resides in the shear-layer at the low-velocity periphery of a jet [Muniz and Mungal, 1997] and has a mean axial velocity of approximately $3S_L$, where S_L is the laminar flame speed of the stoichiometric fuel-air mixture and equal to about 0.4 m/s with methane as the fuel. The mean velocity profiles (shown in Figure 9) suggest the flame leading edge resides at approximately x = 12mm in these images.

Figure 4 indicates the flame has a clear, deleterious effect on the quality of the tomographic-PIV measurement. Outside the illuminated measurement volume (not shown), where noise prevails, the mean 1st-to-2nd correlation peak ratio is approximately 2 – 3. This represents the noise floor for correlation-peak ratio in this measurement. In the non-reacting cases in the left column of Figure 4 the average correlation peak ratio is 7.3 at 40mJ illumination and 11.7 with 25mJ illumination. It is not clear why the case with lower illumination and seed density has a higher mean correlation peak ratio. Despite this peculiarity, however, both cases show relatively uniform ratios through the measurement region. The uniform, high correlation peak ratio in each case is indicative of a robust tomographic PIV measurement.

In contrast, the LJF results in the right column of Figure 4 show a clear drop in peak-ratio in that region of the flow surrounded by the flame sheet. From the jet-centerline (x = 0mm) to a radius of ≈12mm, we observe correlation peak-ratios of ≈5 for both illumination levels. This is above the noise floor but significantly below that observed in the non-reacting jet case. It is important to note that while the flame resides only in the shear-layer, the reduction in correlation peak-ratio is observed across the entire jet. This indicates the effect of the flame on the measurement arises not from any physical changes to the flow velocity but rather from its refraction of light passing along the line-of-sight rays between the measurement volume and the imaging system. As will be shown later, the relatively high SNR achieved in this study overcame this effect, but Figure 4 indicates that in more complex flame configurations, especially those wherein multiple flame sheets cross the line-of-sight between the

measurement volume and the imaging system, refraction may have a significant detrimental effect on the measurement.

Single-Shot Measurements

As an additional check of the vector quality, single-frame measurements were inspected 'by eye'. The goal of these checks was to judge the quality of the vector fields based on physical considerations and prior experience with conventional planar PIV measurements in turbulent LJFs. Figure 5 shows a typical, single-shot measurement acquired with 40mJ illumination. The measurement on the left was acquired in a turbulent non-reacting flow. The one on the right was acquired in a turbulent LJF and corresponds to the raw image shown in Figure 2. The isosurfaces represent the z-component of vorticity, with levels of $-2500s^{-1}$ shown in blue and $+2500s^{-1}$ shown in red. Several important features are evident in this figure.

It has been shown [Watson et al., 1999] that the structure of a turbulent LJF with methane fuel at conditions similar to those used in this study consists of a thin, sheet-like reaction zone that conforms to turbulent flow structures in the shear-layer at the outer periphery of the jet. This thin reaction zone resides on the inner edge (with respect to the jet-centerline) of a layer of hot combustion products. The layer of combustion products typically has a thickness of ≈1 – 2mm. Beyond this layer of hot combustion products, the flame sheet has little effect on the surrounding turbulent flow (Boxx et al, 2014). Comparing the LJF measurement in Figure 5 with the flame luminosity observable in Figure 2, it is clear that the majority of turbulent structure visualized by the vorticity isocontours represents unburned fluid in the jet interior, i.e. fluid away from the influence of the reaction zone. With this in mind, we compare the spatial dimensions and structural features (curvature, axial and radial distribution, etc.) of the vorticity isosurfaces in the reacting and non-reacting flows and note they are quite similar. Although not a quantitative measurement of signal quality, the similarity of the vortical structures visualized in the unburned gas region is consistent with the flow characteristics expected in a turbulent LJF and indicates the flame measurement is plausible from a physical standpoint.

Figure 6 shows profiles of axial-, radial- and azimuthal- (through-plane) velocity from the measurements in Figure 5. The profiles are taken 60mm downstream of the jet-exit, at six different z-locations and show the axial (top), radial (middle) and azimuthal (bottom) component of velocity for each measurement. The purpose of these profiles is to judge the physical plausibility of the measured velocity data in the reacting and non-reacting flow. Inspection of these profiles shows, for example, that features in each profile are identifiable in adjacent planes, consistent with physical flow structures.

It is known from Figure 2 that the flame sheet in this measurement lies at a radial location of approximately x = 12 – 14mm. Consistent with results from Muniz and Mungal (1997), the flow velocity in this region is 1 – 2m/s. The profiles show low gradients of axial velocity in either the x-,y. or z-direction, suggesting a region of low fluid-dynamic shear stress. This too is consistent with what is known about the flow-field of a turbulent LJF at these Reynolds numbers. The profiles of radial velocity show significant high-frequency fluctuation in the region of x ≈ 8 – 12mm. This corresponds to the fluid adjacent to the flame sheet, on the fuel side. Although these fluctuations may be the result of measurement noise, such fluctuations are also consistent with dilatation resulting from heat-release of the flame, i.e. fluid being pushed radially outward as a result of volumetric expansion of hot gases in the direction normal to the flame. Taken together, these observations suggest the velocity measurements acquired in this study are physically plausible.

Vector Validation and Statistics

A quantity of interest in judging the quality of PIV measurements is the percentage of vectors removed and replaced during vector validation. Figure 7 shows profiles representing the percentage of vectors removed during vector validation (integrated over the entire x-y plane and over a full 341 frame acquisition run) vs. z-direction. Figures 7a and 7b show the profiles for the downstream measurement locations. For comparison, Figure 7c shows the percentage of removed/interpolated vectors at the jet-exit measurement location where there is no flame. Several important characteristics are apparent in these profiles.

In the non-reacting flow at the jet-exit the profile is reasonably uniform across the measurement volume, with a decrease in valid vectors toward the lower-intensity wings of the illuminated volume. In the uniform region, 1-2% of vectors were removed during vector validation. This small percentage compares well with conventional stereo-PIV measurements and is a good vector yield in any case. The profiles measured at the downstream locations show considerably less uniformity and a larger percentage of removed/interpolated vectors. In Figure 7a, which corresponds to the downstream measuring location illuminated with 40mJ/pulse, we observe between 2.5% and 8% of vectors are removed through vector validation. In Figure 7b, corresponding to 25mJ illumination, between 3 and 9% of vectors are removed / replaced.

Comparison of the profiles for the reacting- and non-reacting flows in Figures 7 indicates that the presence of a flame does not significantly influence the vector yield for this measurement. At 40mJ illumination, the profiles overlap both in shape and magnitude. With 25mJ illumination, measurement in the LJF actually shows a higher vector yield than the non-reacting jet at the same location. This is consistent with the lower seed particle concentration reported in Table 1. Taken together, relatively high SNR and strong 1^{st}-to-2^{nd} correlation peak ratios, Figure 7 shows the presence of a flame sheet in line-of-sight between cameras and the measurement volume does not inhibit tomographic PIV measurements.

Prior research has shown [Boxx et al., 2014] that the mean and fluctuating velocity profiles of a LJF and those of a non-reacting jet of the same jet-exit and co-flow conditions are almost identical at the mean flame lift-off height. A significant difference between the two would be indicative of an unreliable velocity measurement. Therefore the mean and fluctuating velocity fields were computed from the single-shot tomographic-PIV measurements and the results are presented below.

Jet-Exit Imaging Location

Figure 8 shows the mean velocity field of the LJF measured at the jet-exit with 40mJ/pulse illumination (and laser retro-reflection). The isosurfaces shown correspond to mean axial velocities of 2 m/s (blue), 10 m/s (green) and 21m/s (orange). In this measurement, the instantaneous flame leading edge remained downstream of the measurement volume throughout this imaging run. Also shown in this figure are profiles of the mean and fluctuating (RMS) axial velocity measured at the most upstream location in imaging region, 8mm from the jet-exit.

Figure 8 confirms the quantitative accuracy of the velocity measurements acquired in this study. As expected (based on the ratio of the tube length, L, to inner diameter, d), the mean axial velocity profile in Figure 8 is consistent with that of a fully-developed turbulent pipe flow with mean velocity of 16.5m/s, measured ≈1d downstream of the jet-exit. In addition, both the isocontours shown in Figure 8a and the mean and fluctuating axial velocity profiles shown in Figure 8b confirm that the 341 (statistically independent) tomographic-PIV measurements acquired in a single imaging sequence were sufficient for statistical convergence of the mean velocity in the high-velocity, non-reacting flow at the jet-exit.

Downstream Imaging Location

Figures 9a and 9b show the mean, 3D velocity fields measured with 40mJ/pulse illumination and retro-reflection in the non-reacting and reacting jet, respectively. The isosurfaces represent mean axial velocities of 3m/s (blue), 10m/s (green) and 15m/s (orange). Figures 9c and 9d show profiles of mean axial velocity on the jet centerline plane for increasing downstream distance. Figures 9e and 9f show profiles of fluctuating (root mean square, RMS) axial velocity at the same locations. The profiles of mean axial velocity are clearly statistically converged, showing the expected Gaussian profile that grows linearly in width with downstream distance. The profiles of fluctuating velocity are less well converged but show trends consistent with flow in a turbulent jet with peak fluctuation intensity occurring in the shear-layer and dropping at the jet-centerline.

A comparison of the isosurfaces and profiles of mean and fluctuating axial velocity in Figure 9 shows no clear differences between the velocity fields of the non-reacting and reacting jets. This is consistent with previous research on turbulent LJF, which has shown the presence of the flame has virtually no effect on the mean and fluctuating axial velocity field at the mean flame lift-off height for this jet-exit Reynolds number and co-flow velocity.

Figure 10 shows the same quantities plotted in Figure 9 acquired with 25mJ of laser illumination. Here again, the plots of mean axial velocity have the characteristic Gaussian-shaped profile expected for a turbulent free jet. The profiles of axial velocity fluctuation are less well converged than those illuminated with 40mJ. For example, the profiles for 51mm, 56mm and 60mm downstream in the non-reacting jet show significant (left / right) asymmetry in peak fluctuation magnitude. In addition, the peak fluctuation intensity for the 45mm downstream location appears near the jet-centerline, a clearly non-physical result, given the known flow-field characteristics. Similar, albeit less severe asymmetry is observed in the lifted jet flame profiles. The poorer statistical convergence at 25mJ illumination is consistent with the lower SNR tomographic reconstruction and weaker correlation strength observed earlier, as both would result in a greater number of spurious vectors in each individual measurement. Although vector validation routines can help in identifying and replacing these spurious vectors, it appears that enough remain to impact the statistical convergence of the measurement.

Despite poorer convergence in the regions of peak fluctuation intensity, the profiles of axial velocity fluctuation measured with 25mJ illumination are consistent with those measured with 40mJ. Figure 11 shows the fluctuation intensity profiles for each measurement, 60mm downstream of the jet-exit and overlaid on a single axis. Outside the region of peak fluctuation intensity, the profiles overlap well. We note that the profile measured with 25mJ illumination shows slightly higher magnitude RMS than that measured with 40mJ in the regions of high-intermittency (i.e. in the shear-layer region). This suggests the RMS axial velocity statistics are not as well converged there. The fact that measurements for both the reacting and the non-reacting jets show similar reproducibility, with deviations of similar magnitude in the regions of high velocity fluctuation indicates the presence of a flame in the measurement volume does not significantly affect the overall accuracy of the measurement.

Discussion

The results above demonstrate several important points regarding the application of tomographic-PIV in a turbulent flame. First among these is that it is indeed possible to acquire high-quality volumetric velocity measurements in a turbulent flame. Although several recent studies have demonstrated tomographic velocimetry measurements in a turbulent flame, none have made a thorough test of the quality of the results achieved. The present study shows that not only is it possible to acquire tomographic-PIV measurements in flame but also that it is possible to do so with fidelity approaching that of conventional (planar) stereoscopic-PIV, albeit with reduced spatial resolution.

The key challenge to acquiring tomographic-PIV in a turbulent flame is index-of-refraction variations associated with density variations through the flow. The results above demonstrate that the presence of a flame in the measurement volume and/or in the line-of-sight between the measurement volume and the imaging system does not necessarily prevent a reliable tomographic reconstruction of the 3D particle distributions. The presence of a flame was observed to have a deleterious effect on the volumetric calibration and particle cross-correlations; it was possible nonetheless to acquire usable 3D velocity field measurements. The results also indicate that index-of-refraction variations induced by heat-release at the flame do not prevent the effective use of a single-pass retro-reflecting mirror to increase the effective illumination intensity of the laser. It is not clear from this study if a multi-pass cell of the type described by Ghaemi and Scarano (2010) would be viable for imaging a turbulent flame, but a single-pass retro-reflecting mirror is an effective means by which to increase the illumination of the measurement volume and equalize scattering signals for the cameras (as each views both back and forward scattered radiation).

A major limitation of tomographic-PIV as an effective tool for investigation of turbulence-flame interactions is the achievable volumetric resolution. A reliable tomographic reconstruction of the 3D particle distributions necessitates the use of lower seed density than is typically employed with stereo-PIV. As the maximum achievable spatial resolution is directly linked to the number density of seed particles in the flow, this limits the volumetric resolution achievable. The drop in seed particle density that accompanies volumetric expansion at the flame exacerbates this problem. In the present study, a volumetric resolution of approximately 1.3 - 1.7mm was achieved, which is comparable to most tomographic-PIV studies reported in the literature [Scarano, 2013]. This resolution is a significant fraction of the 8mm jet-exit diameter and the approximately 10mm (FWHM) jet width at the mean flame lift-off height. Although finer resolutions are achievable with increased magnification (i.e., smaller interrogation width and height), for a given aperture and illumination wavelength this comes at a cost of decreased depth of focus. The limited pulse energy of current-generation, kHz-rate DPSS lasers makes increasing one's illumination to compensate for this challenging. The results of this study suggest that the somewhat course spatial resolution achievable with tomographic-PIV will be a significant limitation in many turbulence-flame interaction experiments.

Conclusion

The objective of this study was to test the feasibility of accomplishing tomographic particle image velocimetry (tomographic-PIV) in a turbulent lifted jet flame. As the multi-pass light amplification systems typically employed in kHz acquisition-rate tomographic-PIV studies of non-reacting flows perform poorly in turbulent flames due to index-of-refraction variations, the study was also designed to test the viability tomographic-PIV in a turbulent lifted jet flame (LJF) with pulse energies limited to those achievable with current-generation kHz-rate diode-pumped solid-state laser systems. To this end, a four-camera tomographic-PIV system designed to replicate current-generation laser and imaging technology (albeit operated at 10 Hz) was applied to characterize the flow-field of a turbulent LJF fueled with methane. The measurement volume was $29 \times 28 \times$ 2.7mm in size, providing a reasonable compromise between field of view and spatial resolution. Reconstruction of the 3D particle distributions was accomplished using the multiplicative algebraic reconstruction technique.

To judge the feasibility of this measurement technique in a reacting flowfield, a number of quality checks were applied to determine the signal-to-noise ratio, cross-correlation strength and first-choice vector yields. The results indicate that usable tomographic-PIV measurements in a turbulent flame are possible with laser pulse-energies of 25mJ, despite the presence of a flame both in the measurement volume and the line-of-sight between the measurement volume and the imaging system. Tomographic reconstruction of the 3D particle distribution

was achieved in the LJF with a signal-to-noise ratio (SNR) of 10-12 with 25mJ illumination, and 11-14 with 40mJ. The presence of a flame in the line-of-sight between the measurement volume and the imaging system was seen to have a deleterious effect on the volumetric calibration and the strength of the cross-correlation of the reconstructed particle distributions. The relatively high SNR achieved in this study was sufficient to overcome this effect, and usable 3D velocity field measurements were achieved. The deleterious effect of the flame may be significantly more severe in more complex reactive systems, for example those wherein the flame sheet is highly wrinkled with respect to the line-of-sight between the measurement volume and the cameras, passes through the line-of-sight multiple times or has a large, distributed region of hot gas (e.g. the recirculation zone in a swirl flame) rather than a thin flame sheet. While it is likely that beam steering in some reacting flows (e.g., at high pressures) will make the application of tomographic-PIV difficult or impossible, the present study demonstrates that the tomographic-PIV technique can produce volumetric, three-component velocimetry with high accuracy in at least some turbulent reacting flows.

Acknowledgement

This work was supported by the Air Force Office of Scientific Research (AFOSR) and The European Office of Aerospace Research & Development (EOARD) through Grant FA8655-12-1-2092.

References

R.J. Adrian, Ann. Rev. Fluid Mech. **23**: 261-304 (1991)
S. Pfadler, F. Dinkelacker, F. Beyrau, A. Leipertz, Combust. Flame **156**, 1552–1564 (2009).
S. Pfadler, F. Beyrau, F. Dinkelacker, A. Leipertz, Exp. Fluids **49**, 839–851. (2010)
B. Ganapathisubramani, K. Lakshminarasimhan, N.T. Clemens. J. Fluid Mech. **598**:141-75 (2008).
A. Steinberg, J. Driscoll, S. Ceccio. Exp. Fluids **47**:527-47 (2009)
M. Gamba, N.T. Clemens, O.A. Ezekoye. Meas. Sci. Technol. **24**. 024003 (2013)
G.E. Elsinga, F. Scarano, B. Wieneke, V.W. van Oudheusden, Exp. Fluids **41**, 933-947 (2006).
F. Scarano, Meas. Sci. Technol. **24**. 012001 (2013)
B. Lecordier, C. Gobin, C. Lacour, A. Cessou, B. Tremblais, L. Thomas, L. David. 16th Int Symp on Applications of Laser Techniques to Fluid Mechanics. Lisbon, Portugal, 09-12 July, 2012.
B. Coriton, A.M. Steinberg, J.H. Frank. 8th U. S. National Combustion Meeting. Paper # 070DI0040.
P. Petersson, M. Gesnik, J. Olofsson,V. Jaunet, M. Aldén. Proceedings of the European Combustion Meeting 2013, Paper P3-15, June 25-28, 2013, Lund, Sweden. ISBN 978-91-637-2151-9.
A.K. Prasad. Exp. Fluids, 29:103-116 (2000).
M. Raffel, C.E. Willert, J. Kompenhans. Particle Image Velocimetry, A practical guide. Springer-Verlag. Berlin. 1998.
A. Schröder, R. Geisler, G.E. Elsinga, F. Scarano, U. Dierksheide. Exp. Fluids 44:305–16, (2008)
D. Violato, P. Moore, F. Scarano. Exp. Fluids, 50:1057–1070, (2010)
R.J. Adrian, C.S. Yao. App. Optics. 24:44-52, (1985)
S. Ghaemi, F. Scarano. J. Fluid Mech. 689:317–56, (2011)
L. Muniz, M.G. Mungal. Combust. Flame, 111:16-31 (1997)
I. Boxx, M. Stöhr, C. Carter, W. Meier. Combust. Flame 15:8, 1510-1525 (2010)
L. Muniz, R.E. Martinez, M.G. Mungal, Proc. of the Eighth International Symposium on Applications of Laser Techniques to Fluid Mechanics, Lisbon, Portugal, 411-424. (1996)
D. Han, L.K. Su, R.K. Menon, M.G. Mungal, Proc. of the Tenth International Symposium on Applications of Laser Techniques to Fluid Mechanics, Lisbon, Portugal. (2000).
B. Wieneke. Exp Fluids. 45:549–556 (2008)
J. Westerweel, F. Scarano. Exp. Fluids, 39:1096–1100 (2005)
H.G. Maas, A. Gruen, D. Papantoniou. Exp. Fluids, 15:133-146 (1993)
S. Pfadler, F. Beyrau, A. Leipertz. Opt. Express. 15444. 15:23 (2007).
S. Ghaemi, F. Scarano. Meas. Sci. Technol. 21. 127002 (2010)
I. Boxx, C. Carter, W. Meier. AIAA Science and Technology Forum and Exposition, 2014. National Harbor, USA. AIAA-2014-0316. (2014).

Figures / Captions List

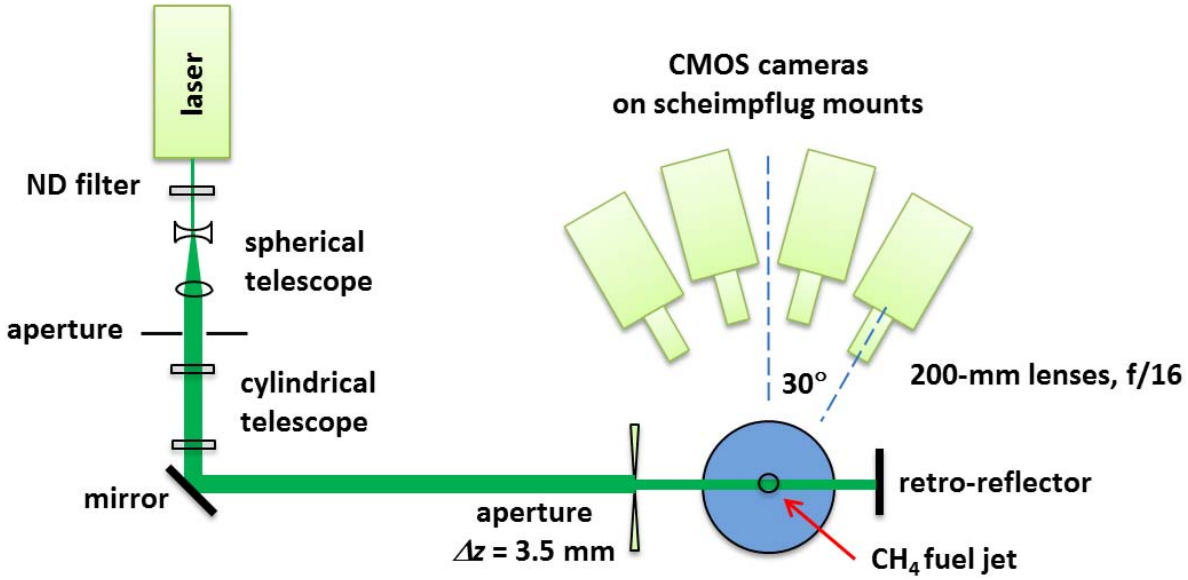

Figure 1 – Experimental Setup

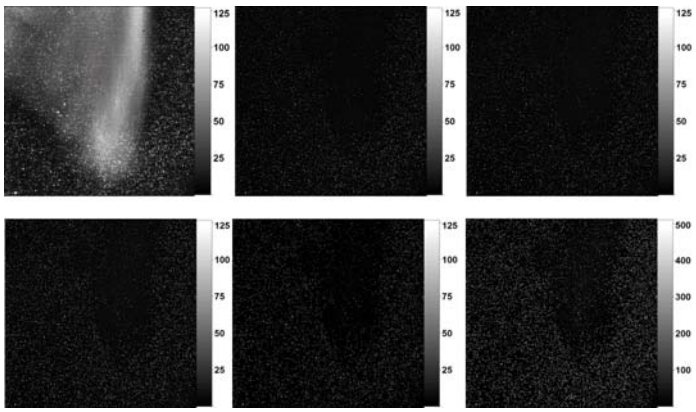

Figure 2. Image pre-processing steps. a) Raw particle image, b) Subtract sliding minimum, c) Local averaging, d) Smoothen/Smoothing, e) Subtract constant background, f) Multiply by constant (note expanded color bar).

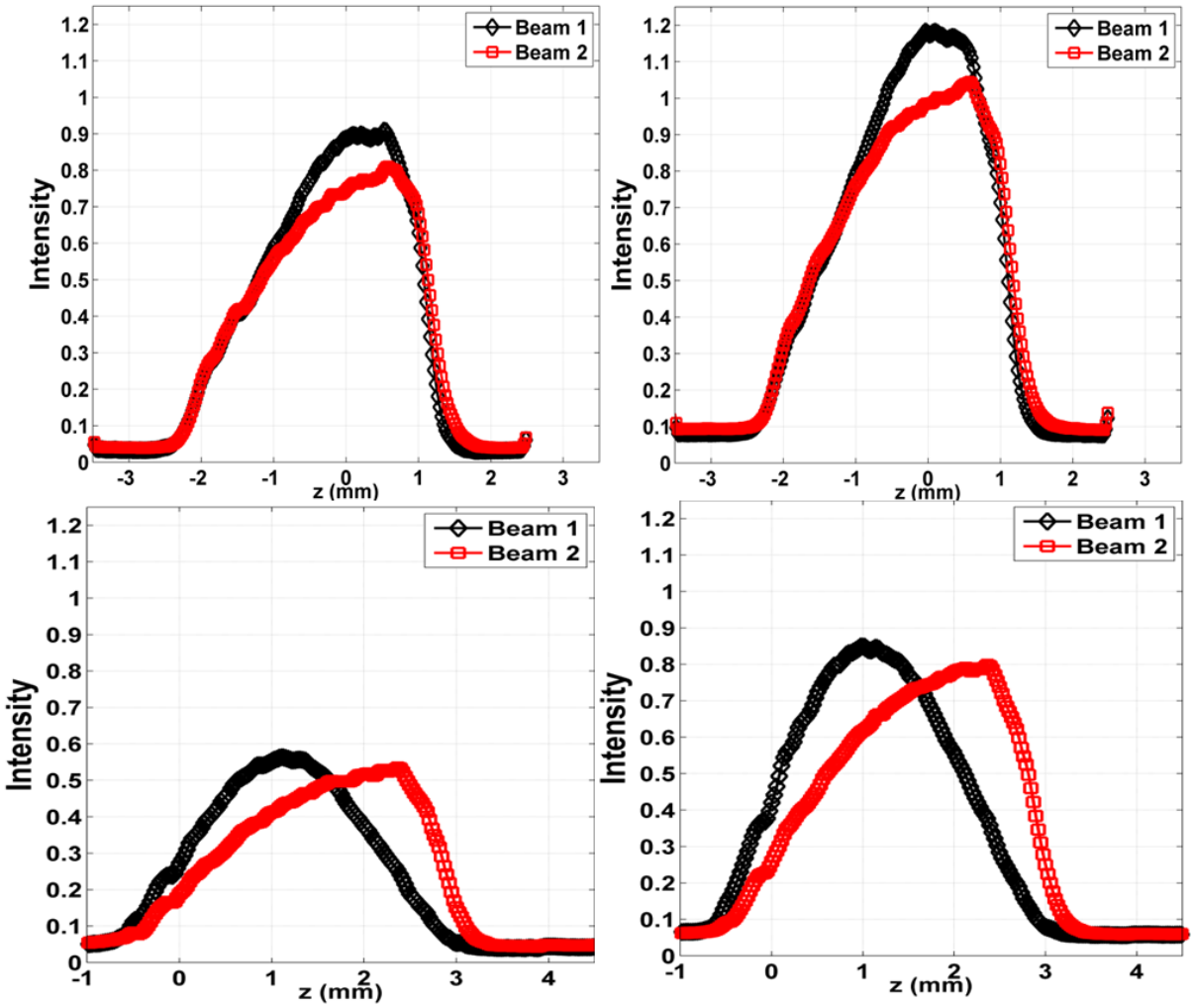

Figure 3. Laser illumination in the z-direction for cases with 40mJ (upper) and 25mJ (lower) illumination. Left - Non-reacting jet, Right – Reacting Jet.

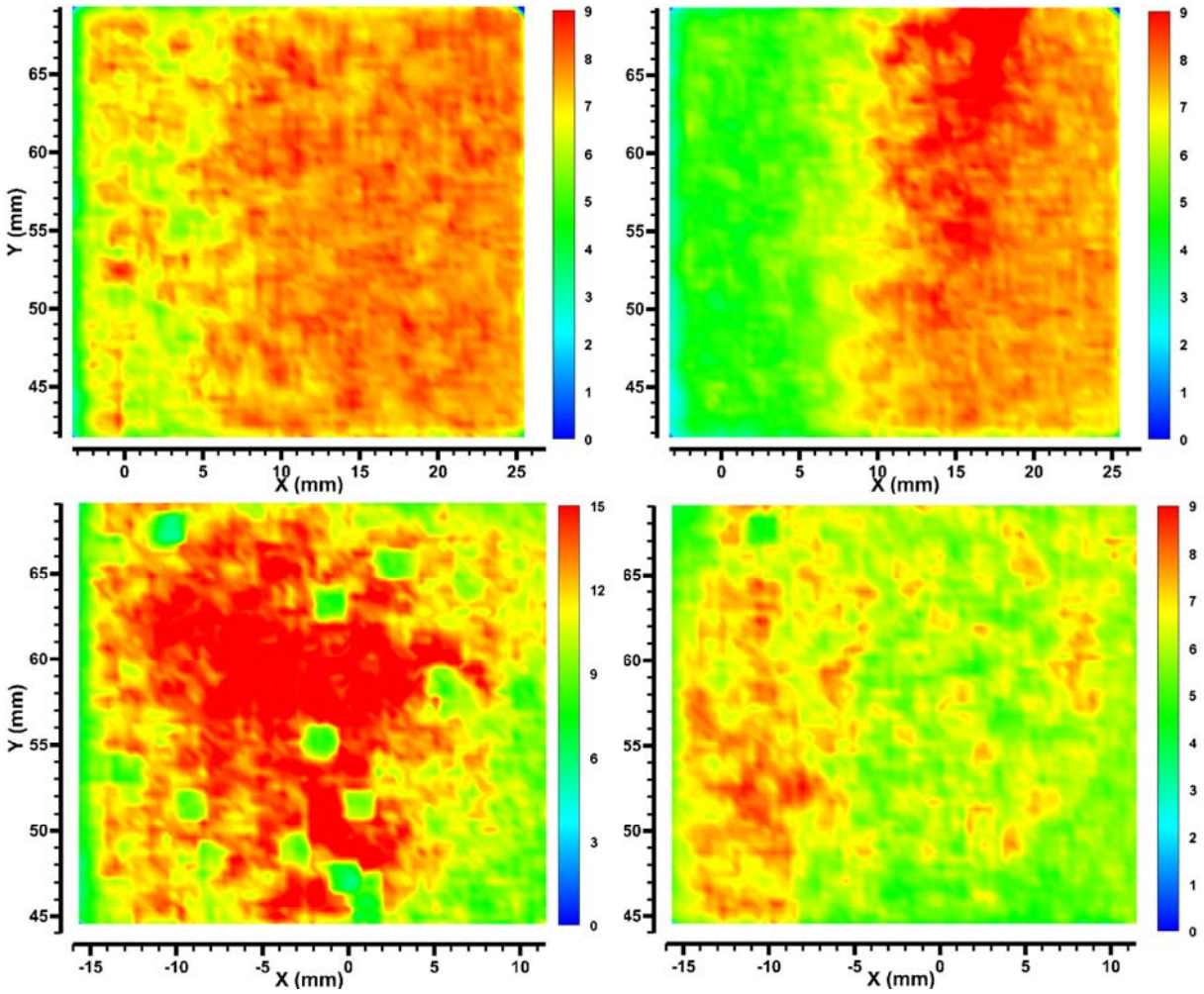

Figure 4. Mean 1st-to-2nd strongest cross-correlation peak ratios. Laser illumination in the z-direction for cases with 40mJ (upper) and 25mJ (lower) illumination. Left - Non-reacting jet, Right - Reacting Jet.

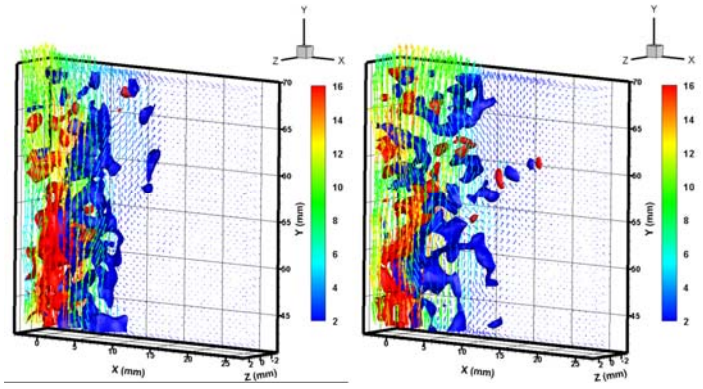

Figure 5. Instantaneous velocity vectors and vorticity isocontours (+/-2500s^{-1}) for 40mJ illumination and laser retro-reflection. a) Non-reacting jet and b) Reacting Jet.

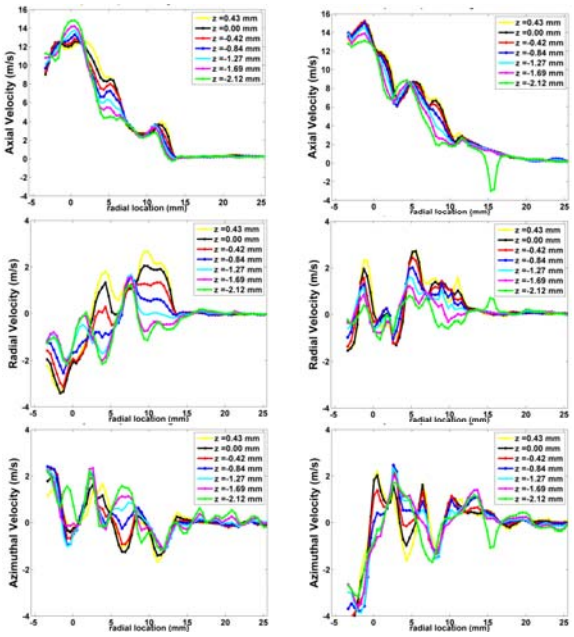

Figure 6. Single-shot profiles of each velocity component. Measured 60mm downstream of jet-exit with 40mJ illumination and laser retro-reflection. Left – Nonreacting jet. Right – Reacting Jet.

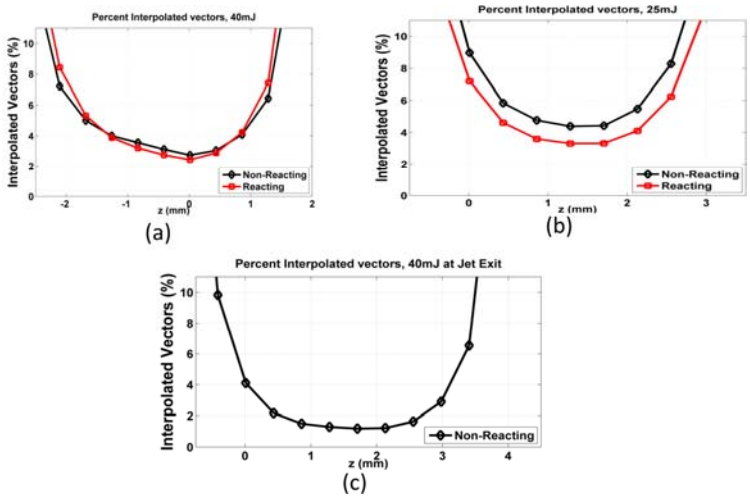

Figure 7. Percentage of vectors removed and replaced in validation. a) Downstream location, 40mJ/pulse. b) Downstream location 25mJ/pulse, c) Jet-exit location (non-reacting).

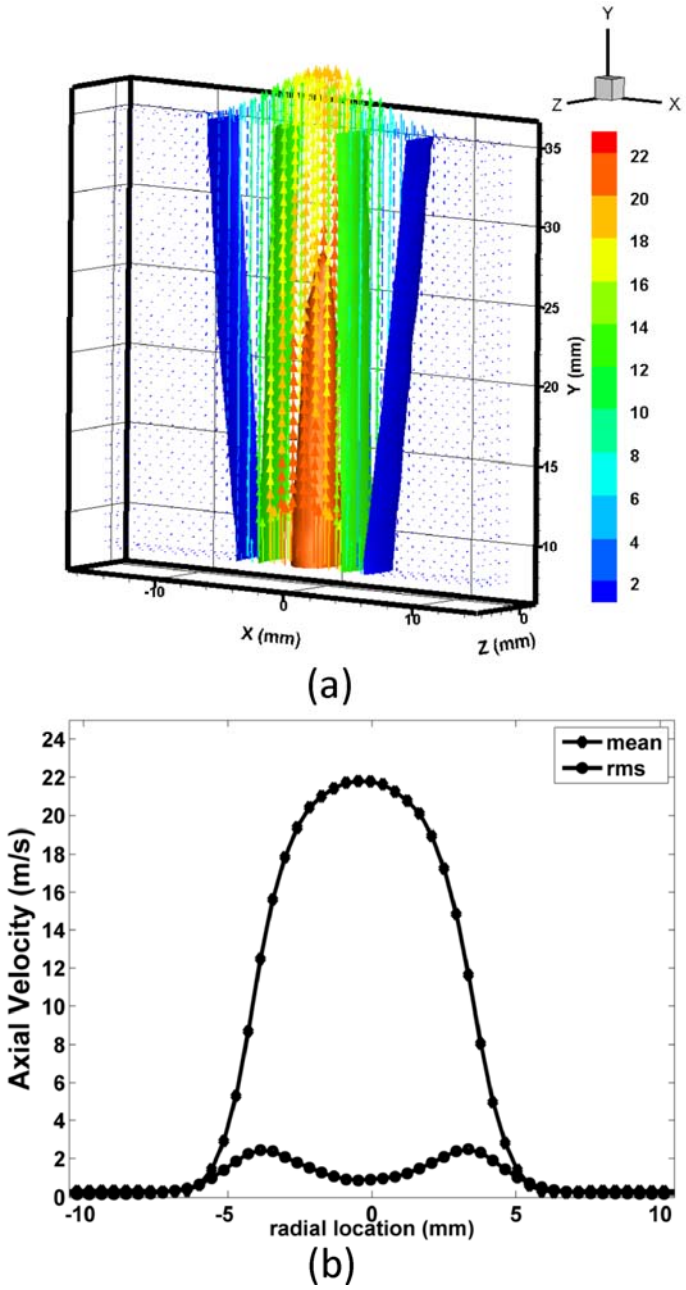

Figure 8. a) Mean axial velocity, 8 - 35mm downstream of the jet-exit. b) Mean and fluctuating (RMS) axial velocity profile 8mm from the jet-exit.

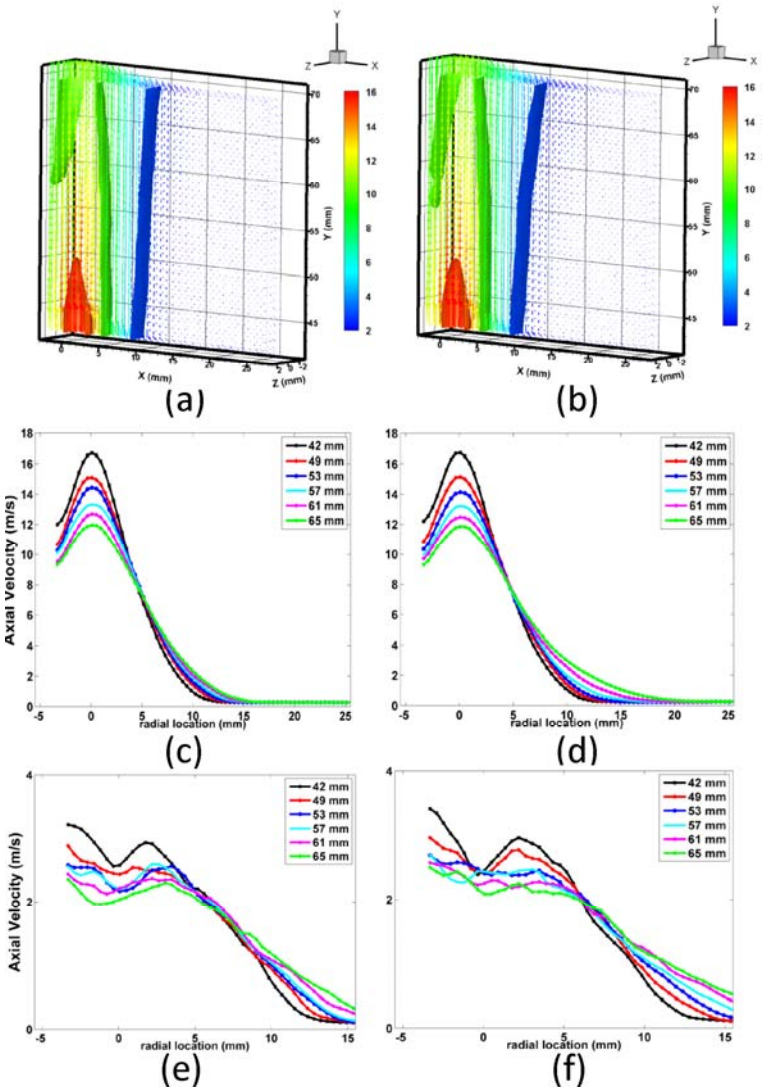

Figure 9. a) Mean axial velocity, 40mJ illumination the Non-reacting jet and b) Reacting Jet; Mean axial velocity profile for increasing downstream distance from the jet-exit in the c) non-reacting and d) Reacting Jets; Fluctuating (RMS) axial velocity profile for increasing downstream distance from the jet-exit in the e) non-reacting and f) Reacting Jets.

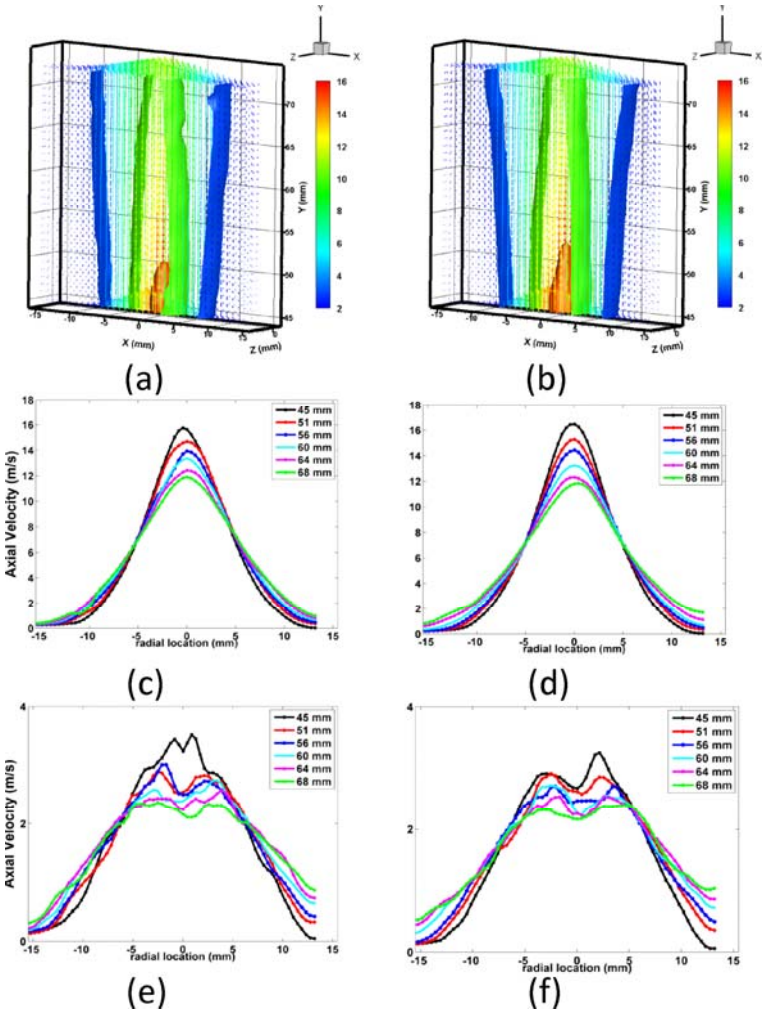

Figure 10. a) Mean axial velocity, 25mJ illumination the Non-reacting jet and b) Reacting Jet; Mean axial velocity profile for increasing downstream distance from the jet-exit in the c) non-reacting and d) Reacting Jets; Fluctuating (RMS) axial velocity profile for increasing downstream distance from the jet-exit in the e) non-reacting and f) Reacting Jets.

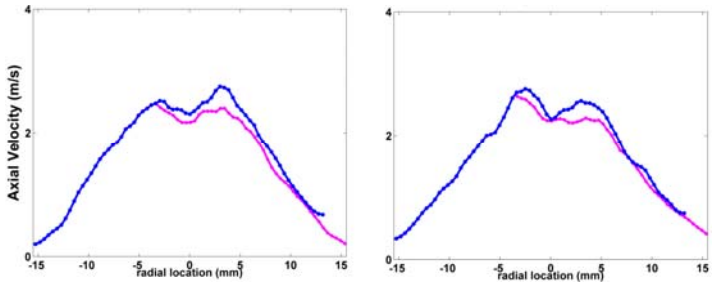

Figure 11. RMS axial velocity profiles, measured 60mm from jet-exit with the purple and blue lines corresponding to 40 and 25mJ illumination, respectively. a) Non-reacting jet and b) Reacting Jet.